



BEN GURION UNIVERSITY OF THE NEGEV

FACULTY OF ENGINEERING

Electrooptical Engineering Unit

**Light-Overtones Interaction with Guided Wave  
Optics Scheme**

by

**Aviad Katiyi**

Supervisor: Dr. Alina Karabchevsky

M.Sc. Thesis

September 2017

## ABSTRACT

Guided wave devices are increasingly becoming an attractive building block in a variety of systems, which is attributed to their unique features of large evanescent field, compactness, and most importantly their ability to be configured according to the required application. This thesis summarizes the study of the evanescent field interaction in waveguides and microfibers devices in different forms and applications, in particular for sensing and detection.

In our work, we explore the excitation of molecular overtones on by evanescent fields on a waveguide. Our method is based on the light-matter interaction enhancement.

A library of theoretically calculated feasible waveguides and microfibers designs is presented and the response of the optimal candidate is studied under the broadband excitation.

Experimental observations are summarized and analyzed in this thesis.

# Contents

<b>Abstract</b>	<b>i</b>
<b>Table of Contents</b>	<b>ii</b>
<b>List of Figures</b>	<b>iv</b>
<b>List of Tables</b>	<b>vi</b>
<b>Nomenclature</b>	<b>vii</b>
<b>1 Introduction</b>	<b>1</b>
1.1 Motivation and project focus . . . . .	1
1.2 State of the art . . . . .	1
1.3 Techniques used . . . . .	4
1.3.1 Numerical modeling . . . . .	4
1.3.2 Fabrication . . . . .	4
1.4 Thesis layout . . . . .	5
<b>2 Background</b>	<b>6</b>
2.1 The fundamentals of guided wave optics . . . . .	6
2.2 Molecular spectroscopy . . . . .	10
2.3 Aromatic amines . . . . .	15
2.4 Tapered guided wave structures . . . . .	16
2.4.1 Fibers . . . . .	16
2.4.2 Waveguides . . . . .	18
<b>3 Computational analysis</b>	<b>20</b>
3.1 Materials dispersion . . . . .	20
3.2 Proposed waveguide structure . . . . .	23
3.3 Waveguide design . . . . .	28
3.3.1 Single mode region . . . . .	29
3.3.2 Sensing region . . . . .	29
3.3.3 Transition region . . . . .	31
3.3.4 Calculated waveguide dimensions . . . . .	32
<b>4 Experimental results</b>	<b>33</b>
4.1 Proof-of-principle experiments . . . . .	33
4.1.1 Spectroscopy of aromatic amines . . . . .	33
4.1.2 Spectroscopy of cancer cell treatment response . . . . .	35

---

<b>5</b>	<b>Summary</b>	<b>38</b>
5.1	Summary . . . . .	38
<b>6</b>	<b>Future plans</b>	<b>40</b>
6.1	Future plans . . . . .	40
<b>7</b>	<b>List of Publications</b>	<b>41</b>
7.1	Journal articles . . . . .	41
7.2	Conference papers . . . . .	41
	<b>References</b>	<b>42</b>

# List of Figures

2.1	Schematic of slab waveguide contains a three-layer system. . . . .	7
2.2	Cross-section of the mode in ridge waveguide with evanescent tail beyond the physical dimensions of the guiding layer. . . . .	10
2.3	Different vibration modes of H <sub>2</sub> O molecule and its excitation frequencies in units of cm <sup>-1</sup> . . . . .	11
2.4	Schematic of the transmittance for different oscillator models. (a) Harmonic oscillator model. (b) Harmonic oscillator model with the heterogeneity of the sample. (c) Anharmonic model. . . . .	11
2.5	Morse potential function for anharmonic vibration compared to harmonic vibration. $\nu_f$ - fundamental frequency. $n\nu_f$ - $n^{\text{th}}$ overtone. $D_e$ - Well depth. . . . .	14
2.6	Molecule chemical formulas: (a) Aniline - C <sub>6</sub> H <sub>5</sub> NH <sub>2</sub> . (b) N-methylaniline - C <sub>6</sub> H <sub>5</sub> NH(CH <sub>3</sub> ). (c) Ammonia - NH <sub>3</sub> . . . . .	15
2.7	Tapered guided wave structures: (a) Ridge waveguide. (b) Fiber. . . . .	16
2.8	Schematic cross-section of the tapered fiber and the illustration of the propagating mode. . . . .	17
2.9	Numerical modeling of microfiber. (a) Fraction of power in the core of the guide and in the evanescent field relative to the total power of microfiber embedded in 1:3 mixture ratio of NMA:Hexane with changing radius for a wavelength of 1.5 $\mu\text{m}$ . (b)-(d) Normalized electric field (EF) of various core radii from Fig. (a). . . . .	18
3.1	The absorption bands of N-methylaniline, hexane, and mixture ratio 2:3, 1:3, and 1:6 of NMA:hexane calculated using Jasco V570 spectrophotometer. . . . .	22
3.2	Dispersion of (a) hexane, (b) 1:3 ratio of NMA:hexane, (c) 2:3 ratio of NMA:hexane, and (d) pure N-methylaniline calculated using Hilbert transform. . . . .	23
3.3	Rendered images of common laterally confined passive waveguide structures: (a) a strip-loaded waveguide, (b) a ridge waveguide, (c) a rib waveguide, (d) a buried waveguide, and (e) a diffused waveguide. The dimensions of the structures considered in this study are labeled. . . . .	24
3.4	Normalized electric field amplitude colormaps for squeezed waveguides embedded in the mixture ratio 1:3 of NMA:hexane for a wavelength of 1.5 $\mu\text{m}$ : (a) slab waveguide, (b) rib waveguide, (c) ridge waveguide, and (d) microfiber. . . . .	26
3.5	Cross-section profiles of normalized electric field amplitudes of the evanescent field in the analyte for squeezed waveguide compared to single-mode waveguides embedded in the mixture for a wavelength of 1.5 $\mu\text{m}$ . (a) Slab waveguide, (b) ridge waveguide, and (c) microfiber. . . . .	27
3.6	Schematic of ridge-tapered waveguide. . . . .	29

---

3.7	Absorption of hexane, N-methylaniline, and different ratio mixtures of NMA:hexane for a sensing region with a width of 350 nm. . . . .	30
3.8	Propagation losses with different guiding layer widths for a wavelength of 1.5 $\mu m$ (a) width of 350 nm and (b) width of 400 nm. . . . .	31
3.9	Different types of taper shapes: (a) linear, (b) parabolic, (c) hyperbolic, and (d) S-type. . . . .	32
4.1	Schematic of the experimental set-up for in-line spectroscopic measurement.	34
4.2	(a) Silicon rib waveguide used in the experiment. (b) Scanning electron micrograph (SEM) image of the waveguide cross-section. . . . .	34
4.3	The transmittance spectra of different samples on silicon rib waveguide. (a) N-methylaniline and aniline. (b) N-methylaniline and mixture ratio 2:3 and 1:3 of NMA:hexane. . . . .	35
4.4	(a) Schematic of the experimental set-up. (b) Microfiber sensing device used in the experiment. . . . .	36
4.5	Normalized transmittance: (a) With time difference of 30 sec. (b) Before and after 24h treatment. . . . .	37

# List of Tables

3.1	Fraction of the power propagating in single-mode waveguide embedded in 1:3 ratio mixture of NMA:hexane for a wavelength of $1.5 \mu m$ [1] . . . .	25
3.2	Fraction of the power carried by the modes of squeezed waveguides embedded in 1:3 ratio mixture of NMA:hexane for a wavelength of $1.5 \mu m$ [1]. . . . .	27

# Nomenclature

## Abbreviations

FDTD	Finite difference time domain
FEM	Finite element method
FoM	Figure of Merit
FTIR	Fourier transform infrared
Hex	Hexane
IR	Infrared
NIR	Near-infrared
NMA	N-Methylaniline
OPD	Optical path difference
OSA	Optical spectrum analyser
SEM	scanning electron microscope
SM	Single mode
SMF	Single mode fiber
SOI	Silicon on insulator
TE	Transverse electric (mode)
TM	Transverse magnetic (mode)

## Mathematical symbols (Latin)

$A$	Complex field amplitude
$a$	Constant for a particular molecule
$B$	Magnetic induction vector
$c$	Speed of light in vacuum

$D$	Diffusion constant
$E$	Electric field vector
$H$	Magnetic field vector
$\hbar$	Dirac constant
$k$	Wave number
$m$	Radial mode-order number
$\tilde{n}$	Complex refractive index
$n$	Refractive index
$n_{\text{eff}}$	Effective (mode) index
$\mathcal{P}$	Cauchy principal value
$P$	Power
$\Re$	Real part
$r$	Location
$\mathcal{S}$	Time average Poynting vector
$s$	Isotropic source term
$t$	Time
$v$	Vibrational quantum number

#### Mathematical symbols (Greek)

$\alpha$	Absorption coefficient
$\beta$	Propagation constant
$\epsilon_r$	Relative permittivity
$\eta$	Power fraction
$\psi$	Wave amplitude
$\phi$	Photon fluence rate
$\kappa$	Extinction coefficient
$\mu_r$	Relative permeability
$\mu_a$	Absorption coefficient
$\nu$	Frequency
$\omega$	Angular frequency
$\chi$	Anharmonicity coefficient

# Chapter 1

## Introduction

### 1.1 Motivation and project focus

The thesis focuses on exploiting the near-infrared (NIR) absorption enhancement in overtones on guided wave structures by increasing the light-matter interaction. The main goal is to study the so far overlooked absorption by molecular vibrations overtones on photonic waveguide in NIR and explore the novel optical architectures for improved sensing schemes. In particular, we explore the tapering of waveguides and microfibers for molecular spectroscopy.

### 1.2 State of the art

Spectroscopy is a technique to investigate the structure of a molecule by the interaction of radiation with matter [2]. The interaction changes the energy of the molecule, resulting in absorption bands in the transmission spectrum. Each electromagnetic region has a different influence on the molecule. Infrared (IR) spectroscopy, which has been available since the 1940s [3], causes vibrations of the atoms in the molecule. IR spectroscopy is a powerful tool for information on a molecule and can be used for liquid, solid, or gaseous samples. IR chip-scale sensors can permit in situ and real-time sensing.

Infrared spectroscopy can be divided into two regions: mid-infrared (MIR) and near-infrared (NIR). The mid-IR ranges from 2.5 to 25  $\mu\text{m}$  [4]. In this region, the radiation excites fundamental vibrational mode, resulting in a well-defined absorption that exhibits a great potential for sensing and molecular detection. The near-IR ranges from 0.8 to 2.5  $\mu\text{m}$  [4]. In this region, the radiation excites overtone and combination vibrational modes. The low absorption coefficient in this region permits high penetration depth and an adjustment of sample thickness. It allows direct analysis of strongly absorbing and highly scattering samples without further pretreatments [5]. Each region has strengths and weaknesses. For example, near-IR can be used for applications with water as a solvent due to low absorption in this region. Mid-IR, on the other hand, can be used for organic functional groups due to well-defined absorption bands in this region.

A method for spectroscopy is direct interaction of the light with the sample. Fourier transform infrared (FTIR) spectroscopy, which is based on interference of radiation between two beams, is one example. Different from a dispersive spectrometer, the sample is illuminated by a broadband beam. An interferometer, usually a Michelson interferometer, is used to change the frequencies in the probe beam through the measurement process by creating an optical path difference (OPD) between the two arms of an interferometer. It results in a high resolution compared to a monochromatic spectrometer. The longer the OPD, the higher the resolution. The output signal of FTIR spectroscopy, called an interferogram, is defined as the intensity as a function of the OPD. It converts into a frequency spectrum by using Fourier transform. FTIR spectroscopy can be used for a variety of applications such as forensics and pharmaceuticals. The latest work showed direct interaction on a slot waveguide. In a slot waveguide, the guiding layer has subwavelength thickness and lower refractive index compared to the surroundings. Due to Maxwell's equation, a strong electromagnetic field will be confined and guided by the lower index guiding layer [6]. A chip-scale sensor using an opto-nano fluidic slot waveguide was used for mid-IR spectroscopy [7]. The guiding layer is the sensing region. The direct interaction enhanced the sensitivity of the optofluidic sensor, which was able to detect common chemicals, such as N-bromohexane and isopropanol.

Another method for spectroscopy is an interaction of the evanescent field with the sample. It has few advantages such as small dimensions and requiring no adjustments of optical or mechanical components [8]. A ring-resonator based sensor is an example of an evanescent field sensor [9]. The resolution of the sensor is defined by the wavelength range between two resonances, and it shows enhanced sensitivity due to the heavy influence of the resonator environment. It can sense temperature, refractive index, and even strain. In addition, a ring-resonator sensor exhibits an enhanced sensitivity compared to the same length of a straight waveguide (factor of 20). Previous work [10] demonstrated the ability to identify the transmittance spectra of N-methylaniline from 1.46 to 1.6  $\mu\text{m}$  with a resolution of 1 nm using microring resonator. Another example of guided wave structure that can be used for spectroscopy is a diffused waveguide. This was used for overtone spectroscopy in the near-IR region [11]. It showed well-defined amine overtone absorption around 1.5  $\mu\text{m}$  due to the slow light phenomena in the diffusive region. It enhanced the absorption by a factor of 300 in N-methylaniline and by a factor of 80 in aniline compared to the expected absorption in the case of ballistic propagation of light in a waveguide.

The aim of the research was to study guided wave optics structures for overtone spectroscopy in the near-IR. Using the near-IR region has few advantages. The main challenge of the overtone spectroscopy compared to probing the fundamental vibrations is the low transition probabilities of the overtones. However, the samples volume can be significantly reduced while probing the overtones compared to probing fundamental vibrations. For example, for the first overtone IR spectroscopy, we need a liquid cell thickness of about one millimeter. While in fundamental IR spectroscopy, we need liquid cell thickness of several microns, which is difficult to obtain [12]. In the research, we focused on enhancing the sensitivity by optimizing the guided wave structure. A tapered structure was chosen for enhancing the sensitivity due to the big fraction of the evanescent field in the squeezed guiding layer. This configuration has availability in detection over a broad spectral range and a label-free sensing ability. It provides improvements over current evanescent-wave sensors such as the ring-resonator sensor [10] and attenuated total reflectance (ATR) crystal.

## 1.3 Techniques used

### 1.3.1 Numerical modeling

Finite element method (FEM) simulations have been conducted using the commercially available COMSOL Multiphysics modeling software in order to design the appropriate guided wave structure and study the physics of this structure. Finite difference time domain (FDTD) simulations have been conducted with the commercially available Lumerical modeling software in order to design and study the optimized configurations to be fabricated and employed in in-line broadband control experiments. The theoretical analysis was complemented by simulations that investigated the guided wave devices' response under broadband control excitation while devices are embedded in the molecular mixture.

### 1.3.2 Fabrication

Two guided wave structures were used for the proof-of-principal experiments: Silicon rib waveguide and tapered fiber.

The silicon rib waveguide had a silicon-on-insulator (SOI) structure. Low-pressure chemical vapor deposition (LPCVD) was employed to deposit thin Si films, at a height of 400 nm, on SOI wafers. Reactive Ion Etching was used to define the channel waveguides by removing the thin Si films.

The tapered fiber was made of conventional single-mode fiber. The fiber was heated by using a filament-based furnace to create a soft area in the silica. The fiber was pulled to create microfiber region in the fiber. The fiber was tapered to microfiber with a diameter of approximately  $2.5 \mu\text{m}$ .

## 1.4 Thesis layout

Chapter 2 explains the basic background of the project, including: theory of guided wave optics, the fundamental physical and mathematical description of molecular overtone vibrations spectroscopy, aromatic amines and tapered fiber.

Chapter 3 introduces the computational analysis for optimal waveguide structure for molecular vibrations overtones spectroscopy. We investigated the characteristics of different parts of the waveguide sensor, including: type of the waveguide, single-mode region, tapering region, and the sensing region. The performance of the optimum design was investigated under near-infrared region.

Chapter 4 shows the experimental results. Through demonstration of the intriguing enhanced molecular overtone absorption and superior optical functionality, two proof-of-principle experiments were performed. The first experiment investigated absorption of aromatic amines using a silicon rib waveguide. The second experiment investigated cancer cells using a tapered fiber.

Chapter 5 summarizes the computational and experiment results. It also presents the conclusions.

Chapter 6 discusses the future plans.

# Chapter 2

## Background

### 2.1 The fundamentals of guided wave optics

In a guided wave optics regime, the light propagates in the medium due to total internal reflection. To enable propagation, the guiding layer needs to have a higher index than the surroundings to allow total internal reflection.

$$\theta_c = \sin^{-1}\left(\frac{n_1}{n_2}\right) \quad (2.1)$$

$$n_2 > n_1 \geq n_3 \quad (2.2)$$

$n_1$ ,  $n_2$ , and  $n_3$  are the refractive indices of the superstrate, guiding layer, and the substrate, respectively.

To calculate the parameters of the mode of guided wave structure, we use Maxwell's wave equation. We solved the wave equation for electromagnetic waves.

$$(\nabla^2 + \beta^2)E(r, t) = 0 \quad (2.3)$$

$$\psi(r, t) = E(r, 0)e^{i\omega t} \quad (2.4)$$

$\nabla^2$  - Laplacian.

$\beta$  - Propagation constant.

$E$  - Electric field vector.

$r$  - Distance.

$t$  - Time.

$\omega$  - Angular frequency.

The structures in guided wave optics are made of a substrate, guiding layer, and superstrate. The basic structure for guiding light is slab waveguide. It is characterized by parallel planar boundaries with respect to one (x) direction as shown in Figure 2.1. It forms the basis for the analysis of practical waveguides of rectangular cross-section.

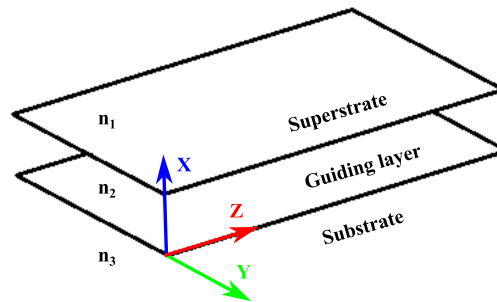


FIGURE 2.1: Schematic of slab waveguide contains a three-layer system.

Solving the Maxwell wave equation for a slab waveguide gives a basic understanding of the mode's behavior. We solve the wave equation to find the (a) guiding modes, (b) propagation constants, and (c) effective indices which are important for guided wave optics. Assuming propagation of the plane wave and the dimensions of the slab waveguide, we get the following equation:

$$\partial^2 E(x, y) / \partial x^2 + (k^2 n_i^2 - \beta^2) E(x, y) = 0 \quad i = 1, 2, 3 \quad (2.5)$$

$i$  - Number of layer.

The solution of Maxwell's equation requires discrete values of propagation constant  $\beta$ , resulting in a limited number of guided modes. The range of the propagation constants of the guided modes are defined by the effective refractive index. The effective mode index is the refractive index of the mode. It results in a slightly different propagation

velocity of the mode in the guiding layer. The refractive index is a function of the light velocity, resulting in a different effective index of each mode. For the specific mode to be guided and confined in the guiding layer, it needs to fulfill the following range for the effective index:

$$n_3 < n_{\text{eff}} < n_2 \quad n_{\text{eff}} = \beta_m/k \quad (2.6)$$

$n_{\text{eff}}$  - Effective mode index.

$m$  - The mode order.

Solving the wave equation for the effective index range for guided modes gives the following solutions for the slab waveguide:

$$E_y(x) = Ae^{-q(x-d_g)} \quad \rightarrow \quad d_g < x < \infty \quad (2.7)$$

$$E_y(x) = B \cos(hx) + C \sin(hx) \quad \rightarrow \quad 0 \leq x \leq d_g \quad (2.8)$$

$$E_y(x) = De^{-px} \quad \rightarrow \quad -\infty < x < 0 \quad (2.9)$$

$$q = \sqrt{\beta^2 - k^2 n_1^2}$$

$$h = \sqrt{k^2 n_2^2 - \beta^2}$$

$$p = \sqrt{\beta^2 - k^2 n_3^2}$$

$d_g$  - Guiding layer thickness.

$k$  - Wave number.

A, B, C, and D are defined from the boundary conditions.

Beyond the physical dimensions the guiding layer, the field is decaying exponentially. In the guiding layer there is a sinusoidal solution, which shows that the mode is confined and guided in the guiding layer.

Another possible mode type is the radiation mode [13]. When the effective index is smaller than the refractive index of the substrate, a radiation mode is formed. Radiation modes radiate from the guiding layer to the surroundings. The substrate radiation mode

forms when  $n_1 < n_{\text{eff}} < n_3$ . It radiates to the substrate, causing the mode to decay after a short distance. However, this mode can be used for coupling application [14]. To solve the wave equation for the tapered fiber and the rib waveguide we used numerical tools, since there is no simple analytical solution for these guided wave structures.

During the propagation, a fraction of the field propagates beyond the guiding layer and vanishes in the direction perpendicular to the direction of  $\vec{k}$ , which is called the evanescent field. As a result of propagating outside the guiding layer, the evanescent field can interact with the surroundings. The fraction of the evanescent field in the analyte can be calculated using time average Poynting vector [15].

$$\text{FoM} = \eta_{\text{analyte}} = \frac{P_{\text{analyte}}}{P_{\text{total}}} = \frac{\iint_{\text{analyte}} S dA}{\iint_{-\infty}^{\infty} S dA} \quad (2.10)$$

$$\mathcal{S} = \frac{1}{2} \Re\{E \times H^*\} \quad (2.11)$$

$\eta$  - Power fraction.

$P$  - Power

$\mathcal{S}$  - Time average Poynting vector.

$A$  - Area.

$\Re$  - Real part.

$E$  - Electric field vector.

$H$  - Magnetic field vector.

This equation can be used to compare and to assess the waveguide architectures for absorption overtone spectroscopy. The FoM is defined as the power in the evanescent field over the total power carried by the mode.

Figure 2.2 shows the cross-section of a TE fundamental mode in a ridge waveguide. The guiding layer edges are defined by the dotted lines. It clearly shows the evanescent tail that propagates outside the guiding layer. This is the part of the mode that interacts with the surroundings.

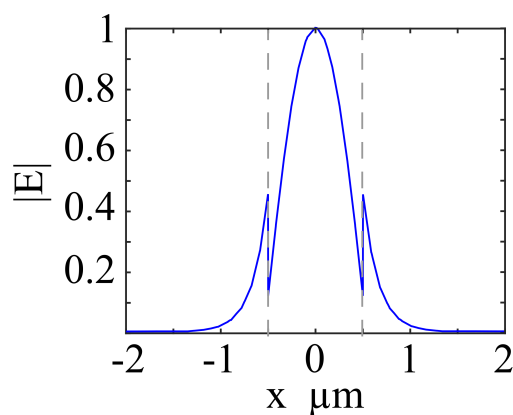


FIGURE 2.2: Cross-section of the mode in ridge waveguide with evanescent tail beyond the physical dimensions of the guiding layer.

## 2.2 Molecular spectroscopy

Spectroscopy focuses on the interaction between light and matter. The interaction causes absorption or emission of radiation. It gives information about different aspects of the molecule structure. The interaction results in change in the energy of the molecule. Each molecule can have five types of energy: translational energy, rotational energy, vibrational energy, electronic energy, and spin energy. Each type of energy appears in a different region in the electromagnetic spectrum and gives different information about the molecule.

Infrared spectroscopy is certainly one of the most important analytical techniques available to today's scientists. Illumination of a molecule in the IR spectrum results in the molecule transition to higher vibrational energy levels.  $v$  is the energy level, which is also called the vibrational quantum number [16]. Each bond can vibrate in different modes, stretching modes and bending modes, which appear as absorption in different regions in the IR spectrum. Figure 2.3 shows examples of different vibration modes of  $\text{H}_2\text{O}$  molecules and their excitation in wavenumber units.

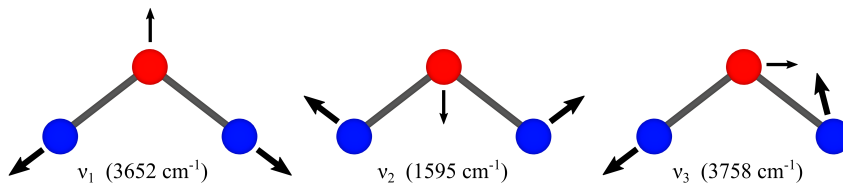


FIGURE 2.3: Different vibration modes of  $\text{H}_2\text{O}$  molecule and its excitation frequencies in units of  $\text{cm}^{-1}$ .

Figure 2.4 summarizes the absorption in different vibration models that will be explained.

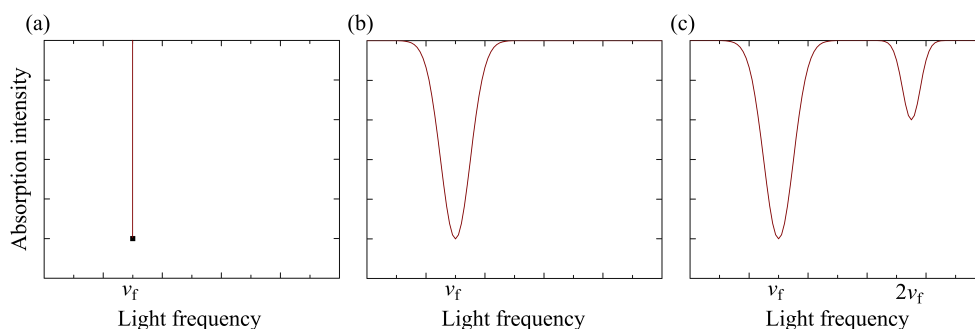


FIGURE 2.4: Schematic of the transmittance for different oscillator models. (a) Harmonic oscillator model. (b) Harmonic oscillator model with the heterogeneity of the sample. (c) Anharmonic model.

The basic model for molecule vibrational mode is the harmonic model. It approximates the vibration forces to spring forces. The Schrodinger equation for the simple harmonic oscillator is given by:

$$\varepsilon_v = \left(v + \frac{1}{2}\right) \hbar \sqrt{\frac{k}{\mu}} \quad (2.12)$$

$$\mu = \frac{m_1 \cdot m_2}{m_1 + m_2} \quad (2.13)$$

$k$  - Force constant.

$\mu$  - Reduced mass.

Transition probability describes the chance of transition from lower to higher energy levels. It defines by

$$R_{i,j} \propto \int \psi_i M \psi_j d \quad (2.14)$$

$\psi$  - Wave equation.

$M$  - Transition moment operator.

Due to the selection rule, only transition of  $\Delta v = \pm 1$  is allowed in the harmonic model. The energy differences between the adjacent energy levels are constant, resulting in the absorption of only a photon with the exact energy that fits the frequency of the oscillator -  $\nu_0$ , as shown in Figure 2.4a. The frequency that leads to the transition from  $v=0$  to  $v=1$  is called the fundamental frequency. Theoretically, in the harmonic model the absorption spectra occur at a discrete frequency with zero width. However, practically, the absorption has non-zero width along the spectrum. This occurs because the harmonic model is correct for a single diatomic molecule or identical diatomic molecules. In reality, the diatomic molecules aren't identical and act differently. The molecule is in a heterogeneous solution. Each molecule is influenced slightly differently by the surroundings. As a result, the vibration frequency for the same transition, for example the fundamental frequency, is a little shifted in different molecules, resulting in broadening of the absorption, as shown in Figure 2.4b.

The biggest different is that molecular vibration motion is basically an anharmonic oscillator. Anharmonic models influence the spectra in few ways. First, the energy differences between the adjacent energy levels are slightly different. This results in a group of absorptions of the same  $\Delta v$  (for example:  $0 \rightarrow 1$ ,  $1 \rightarrow 2$  and  $2 \rightarrow 3$ ), which results in broadening. Second, the transition rule of the harmonic model is not applied in the anharmonic model, which allows vibration transitions of  $\Delta v \neq 1$ . Few absorption bands will appear in the spectrum, as shown in Figure 2.4c. The frequencies that result in those transitions are called overtones or higher harmonics. Due to the lower probability of the overtone transition, adjacent overtones having low intensity generally decrease by a factor of 10 [3].

The Morse model is a better approximation for the vibrational mode of the molecule. Anharmonic oscillator energy levels are approximated by the Morse potential function.

$$V = D_e(1 - \exp[-a(r - r_e)])^2 \quad (2.15)$$

$D_e$  - Well depth.

$a$  - Constant for a particular molecule.

$r$  - Distance between atoms.

$r_e$  - Equilibrium bond distance.

for  $0 \rightarrow v$  transition, the frequency  $\nu$  for absorption is [16, 17]:

$$\nu_{0,v} = \nu_0 \cdot v - v(v+1)\chi \cdot \nu_0 \quad (2.16)$$

$$\nu_0 = \frac{1}{2\pi c} \sqrt{\frac{k}{\mu}} \quad (2.17)$$

$$\mu = \frac{m_1 \cdot m_2}{m_1 + m_2} \quad (2.18)$$

$v$  - Vibrational quantum number.

$\chi$  - Anharmonicity coefficient.

$c$  - Speed of light in vacuum.

$k$  - Force constant.

$\mu$  - Reduced mass.

Figure 2.5 shows the energy levels calculated by Morse potential function for the anharmonic oscillator compared to the harmonic oscillator.

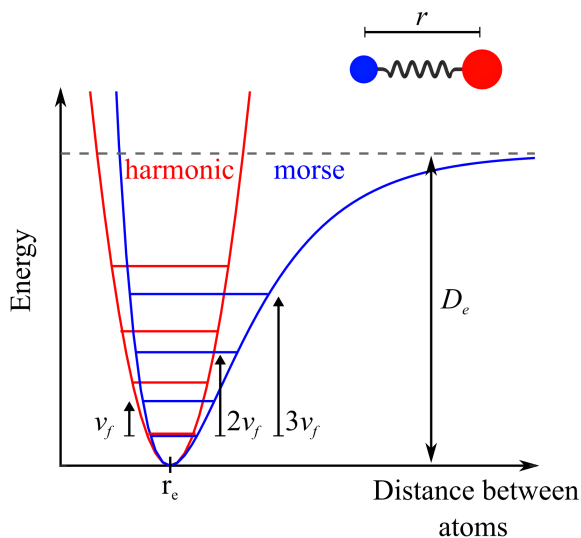


FIGURE 2.5: Morse potential function for anharmonic vibration compared to harmonic vibration.  $\nu_f$  - fundamental frequency.  $n\nu_f$  -  $n^{\text{th}}$  overtone.  $D_e$  - Well depth.

Figure 2.5 shows the difference between the models. In contrast to the constant energy level difference in harmonic, in Morse function the adjacent energy levels are varying and getting smaller. For example, the energy for  $0 \rightarrow 1$  transition is a little bigger than the energy for  $1 \rightarrow 2$  transition. Morse potential also includes the effects of bond breaking when reaching the dissociation energy, which isn't included in the harmonic model.

Studying these absorption bands allows for understanding of the molecular structure and dynamics.

The common region from IR spectroscopy is the mid-infrared (MIR) region. Its big advantage is the excitation of the fundamental vibration mode. The fundamental mode has high absorption that eases the identification of the molecules' bonds. However, it's complicated for a chip size sensor due to the expensive equipment, such as light sources and detectors, in this region. Our method uses the near-infrared (NIR) region for vibrational spectroscopy. This region involves excitation of overtones vibration modes, which have low probability to occur. As a result, the intensity decreases by a factor of 10 between one overtone to the next [3]. Although there is low absorption of the overtones compared to the fundamental, the advantage of the NIR is the matching to the telecommunication region. Its benefits include affordable equipment, materials, and light sources due to its traditional use for optics telecommunication.

## 2.3 Aromatic amines

Amine is a derivative of ammonia, which is shown in Figure 2.6c. Amine can appear in three configurations: primary, secondary, and tertiary amine. These types represent how many hydrogen (H) atoms of the ammonia are replaced by a substituent. Amines are widely used in biology and medicine researches. Aromatic amines have a first overtone of N-H in  $1.5 \mu\text{m}$  [18], which fits the telecommunication region. Figure 2.6 shows the molecular chemical formula of (a) aniline, (b) N-methylaniline, and (c) ammonia.

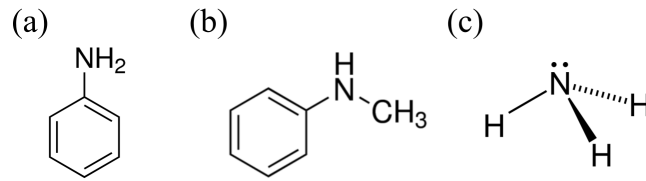


FIGURE 2.6: Molecule chemical formulas: (a) Aniline -  $\text{C}_6\text{H}_5\text{NH}_2$ . (b) N-methylaniline -  $\text{C}_6\text{H}_5\text{NH}(\text{CH}_3)$ . (c) Ammonia -  $\text{NH}_3$ .

In our project, we investigate N-methylaniline (NMA), aniline, and mixtures of N-methylaniline with hexane.

Aniline is a primary aromatic amine that is made of a phenyl ring bound to a primary amine as shown in Figure 2.6a. Aniline and its derivatives are widely used in the dyes industry and pharmaceuticals [19]. Aniline was perhaps first handled during the 18<sup>th</sup> century. The aniline molecule has 14 atoms and  $3n - 6 = 36$  normal modes of vibration. Since vibrational overtones and combination modes are infrared active they can be studied by near-infrared spectroscopy. For example, aniline has vibrations of aryl C-H and N-H. C-H first and second overtones are around  $1.685 \mu\text{m}$  and  $1.143 \mu\text{m}$ , respectively. N-H first overtone is around  $1.507 \mu\text{m}$  [20].

N-methylaniline is an aniline derivative. It is made of a phenyl ring bound to a secondary amine as shown in Figure 2.6b. It is made of a methyl group bound to aniline with an N-bond (as shown in the chemical formula). N-methylaniline has vibrations of aryl C-H and N-H. C-H first and second overtones are around  $1.683 \mu\text{m}$  and  $1.141 \mu\text{m}$ , respectively. N-H first overtone is around  $1.497 \mu\text{m}$  [21]. The absorption band near  $1.5 \mu\text{m}$  is slightly narrower than the absorption band of aniline. The broadening of aniline is

caused by a combination mode that appears near the first N-H overtone [20]. In higher overtones the different absorption peaks are separated.

## 2.4 Tapered guided wave structures

In an IR sensor, the interaction between the evanescent field and the analyte is needed for excitation of vibrational modes. In single-mode dimensions, the fraction of the evanescent field is very low. Low evanescent field decreases the interaction between the evanescent field and the analyte, resulting in low absorption and harming the sensitivity. Squeezing of the guiding layer decreases the confinement of the mode and a higher fraction of the power will propagate outside the guiding layer. This will improve the interaction with the analyte and improve the ability to identify the molecule absorption.

We found that squeezed waveguide and microfiber architectures, as shown in Figure 2.7 [1], allow for the enhanced evanescent light-molecule interaction resulting in increased FoM.

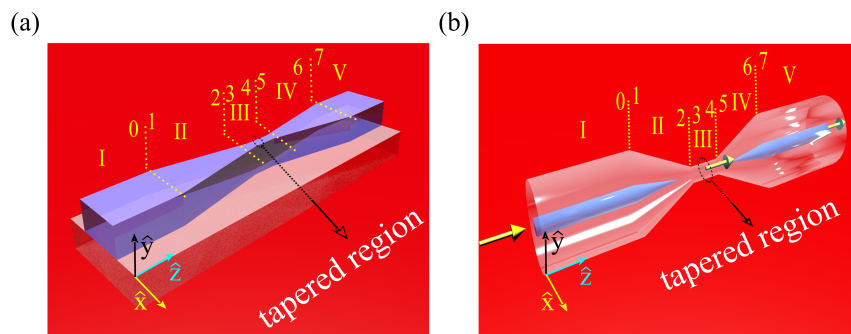


FIGURE 2.7: Tapered guided wave structures: (a) Ridge waveguide. (b) Fiber.

### 2.4.1 Fibers

A particular case of tapered waveguide is a tapered fiber as shown in Figure 2.7b. Tapered fiber can be made of a commercial silica fiber. Optical fiber is heated up locally to the melting temperature of the fiber material. During the heating and stretching a smaller diameter of the fiber is created. The squeezed fiber of micrometer dimensions is called microfiber. When the microfiber is few time the wavelength, the cladding becomes

the guiding layer. When the cladding diameter is getting smaller, a bigger fraction of the power propagates outside the fiber, as shown in Figure 2.8. Therefore, such a tapered fiber is a good candidate for sensing and detection.

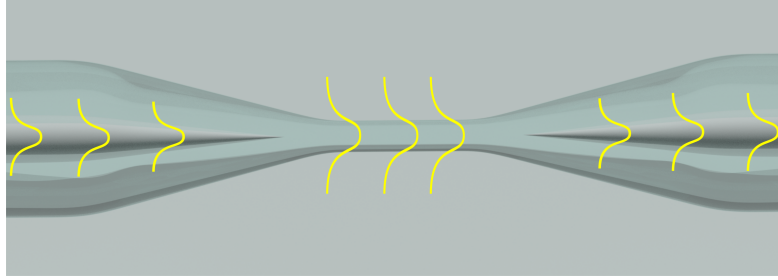


FIGURE 2.8: Schematic cross-section of the tapered fiber and the illustration of the propagating mode.

Due to the surrounding of air, the microfiber is multi-mode. To gain low propagation losses and intermodal coupling, energy transfer between the fundamental mode of the core to higher order cladding modes, the fiber needs to be tapered slowly. It calls adiabatic taper [22]. The length of the adiabatic taper is related to the propagation constants of the modes. This length named beat length.

$$L_b = \frac{\pi}{\beta_1 - \beta_2} \quad (2.19)$$

When the length of the tapered region is longer than the beat length, the fundamental mode will propagate without influence and the power will couple to the fundamental mode in the microfiber region.

Figure 2.9a [23] shows the evolution of the power fraction  $\eta$  with fiber radius  $r$  when the microfiber is embedded in a 1:3 mixture ratio of NMA:Hexane. As the microfiber radius decreases the fraction of the evanescent field increases. Figures 2.9b - 2.9d show the normalized mode profile of microfiber with different fiber radii.

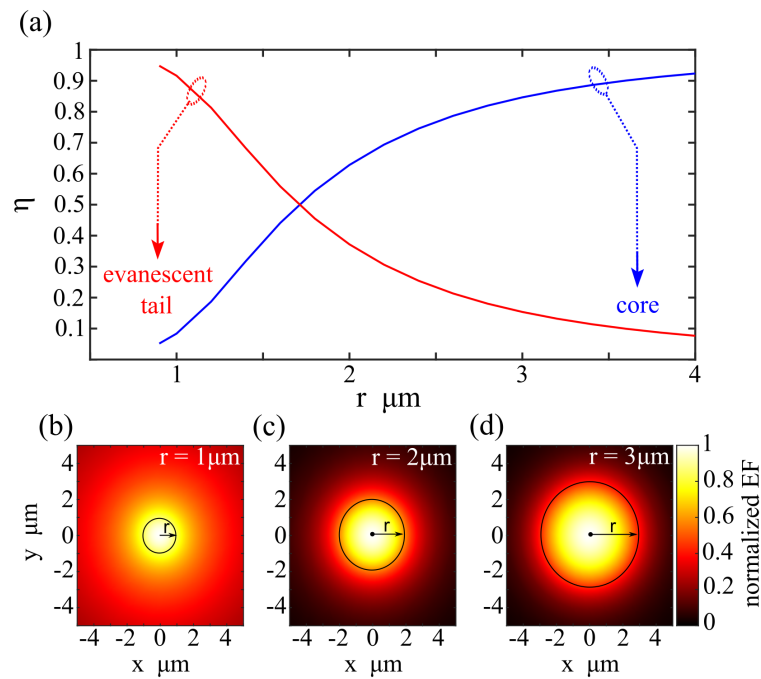


FIGURE 2.9: Numerical modeling of microfiber. (a) Fraction of power in the core of the guide and in the evanescent field relative to the total power of microfiber embedded in 1:3 mixture ratio of NMA:Hexane with changing radius for a wavelength of  $1.5 \mu\text{m}$ .

(b)-(d) Normalized electric field (EF) of various core radii from Fig. (a).

It shown in Figure 2.9 that smaller radius increases the fraction of the evanescent field.

One drawback of tapered fiber is the silica low refractive index ( $n = 1.445$ ). To fulfill the guiding wave condition, the index of the analyte needs to be smaller compared to the index of the fiber core. This criterion results in limitation of the variety of analytes that can be checked in tapered fiber.

However, the major drawback of such a configuration is the lack of durability. The microfiber region is very fragile and can break easily. In addition, some materials can be appended in the microfiber due to cracks which are created in the fabrication process. This will harm the following samplings of the fiber and will give false information. This makes the tapered fiber a single-use sensing device.

## 2.4.2 Waveguides

Another structure that can be used for sensing is a tapered waveguide, as shown in Figure 2.7a. In a tapered waveguide, the guiding layer adiabatically decreases. In the

squeezed region the fraction of the evanescent field increases. The squeezed region is the sensing area.

The advantage of a tapered waveguide is its robustness and inertia to environmental changes.

# Chapter 3

## Computational analysis

### 3.1 Materials dispersion

The complex refractive index describes the response of the material to light. It contains a real part and an imaginary part that describe different characteristics.

$$\tilde{n} = n + i\kappa \quad (3.1)$$

$\tilde{n}$  - Complex refractive index.

$n$  - Refractive index.

$\kappa$  - Extinction coefficient.

The real part is called the refractive index. It describes the decreasing of the light velocity in a material.

$$n = \frac{c}{v} = \sqrt{\mu_r \epsilon_r} \quad (3.2)$$

$c$  - Speed of light in a vacuum.

$v$  - Speed of light in a material.

$\epsilon_r$  - Relative permittivity.

$\mu_r$  - Relative permeability.

The imaginary part is the extinction coefficient of a material, which is related to the attenuation when the wave propagates in a material. Spectroscopy usually measures the absorption of a material. The extinction coefficient can be calculated from the absorption coefficient by the following relation:

$$\kappa(\omega) = \frac{c \cdot \alpha(\omega)}{2\omega} \quad (3.3)$$

$\alpha$  - Absorption coefficient.

$\omega$  - Angular frequency.

Each material has a refractive index that varies with the frequency of the light. This phenomenon is called the dispersion. Most of the transparent material, such as glass, have a nearly constant refractive index. Our investigated materials have absorption that influences the refractive index. The complex refractive index of the analytes is essential for designing a photonic device.

In previous work [11], the absorption of N-methylaniline, hexane, and their mixtures were calculated using a Jasco V570 spectrophotometer recorded at room temperature of  $21 \pm 2$  °C in quartz cuvette path length of 1 mm. The sample was illuminated by wavelength range of 1-2  $\mu m$ . The absorption coefficient was calculated by Beer-Lambert law.

$$I_z = I_0 \cdot e^{-\alpha z} \quad (3.4)$$

$z$  - The length of the sample.

Figure 3.1 shows the absorption bands of N-methylaniline, hexane, and mixture ratios 2:3, 1:3, and 1:6 of NMA:hexane that were calculated using Jasco V570 spectrophotometer. The measured absorption of the samples can be used to calculate the refractive index.

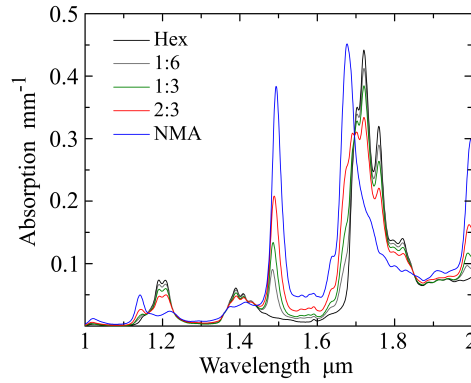


FIGURE 3.1: The absorption bands of N-methylaniline, hexane, and mixture ratio 2:3, 1:3, and 1:6 of NMA:hexane calculated using Jasco V570 spectrophotometer.

Kramers–Kronig (KK) relations, a special form of Hilbert transforms, are mathematical equations that connect the real and the imaginary parts of linear complex optical functions [24]. They can be used for a few calculations such as susceptibility, dielectric function, index of refraction, and reflectivity. For calculating the refractive index from the extinction coefficient that was found by the spectrophotometer, we used the following K-K relations:

$$n(\omega) - 1 = \frac{2}{\pi} \mathcal{P} \int_0^{\infty} \frac{\omega' \kappa(\omega')}{\omega'^2 - \omega^2} d\omega' \quad (3.5)$$

$$\kappa(\omega) = -\frac{2\omega}{\pi} \mathcal{P} \int_0^{\infty} \frac{n(\omega') - 1}{\omega'^2 - \omega^2} d\omega' \quad (3.6)$$

$\mathcal{P}$  - Cauchy principal value.

$\omega$  - Angular frequency.

The major obstacle of using Kramers-Kronig relations is the integration over all frequencies, whereas the spectrophotometer measured the absorption for a finite range. To overcome this problem, we implemented the transform using Hilbert transform in Matlab. Hilbert transform allows calculating the refractive index with finite absorption spectrum. When using Kramers-Kronig relations or Hilbert transform on a finite spectrum, an error can occur in the lower several hundred wavenumbers [25]. The refractive index was calculated for larger range (1 – 2  $\mu m$ ) than the needed range (1.2 – 1.7  $\mu m$ ) so the error will be in the unused region.

We calculated the refractive index in Matlab using Hilbert transform. Figure 3.2 shows the dispersion of N-methylaniline (NMA), hexane (Hex), and mixtures of N-methylaniline with hexane [1]. Figure 3.2a shows the dispersion of hexane. Figure 3.2b and Figure 3.2c show the dispersion of 1:3 and 2:3 ratios of NMA:hexane, respectively. Figure 3.2d shows the dispersion of pure N-methylaniline molecule.

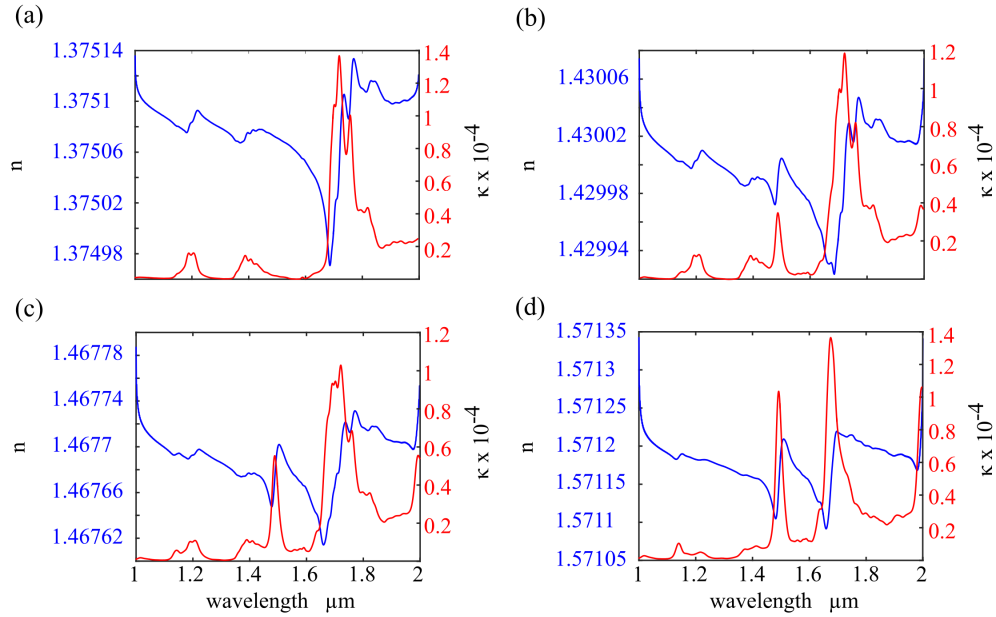


FIGURE 3.2: Dispersion of (a) hexane, (b) 1:3 ratio of NMA:hexane, (c) 2:3 ratio of NMA:hexane, and (d) pure N-methylaniline calculated using Hilbert transform.

### 3.2 Proposed waveguide structure

To gain a deeper understanding of the differences between the waveguides and finding the optimal waveguide structure for overtone absorption, we systematically studied the waveguide structures. The waveguide structures we studied were a slab waveguide, a strip-loaded waveguide, a ridge waveguide, a rib waveguide, a buried waveguide, and a diffused waveguide.

When multiple modes propagate through the waveguide, the energy of the incident wave is non-uniformly divided between the modes. Higher-order modes propagate at bigger inclination angles, given by electromagnetic wave analysis [26], and exhibit scattering losses due to surface defects that are induced during the fabrication routines. The variety of modes also raises the modal dispersion, which decreases the signal-to-noise

ratio. Hence, we consider single-mode waveguides in our numerical model. Numerical modeling has been performed by using a finite-element method (FEM) implemented in COMSOL Multiphysics 5.2. We defined the waveguide dimensions for a single-mode operation while considering the practical fabrication limitations.

The single-mode structures are shown in Figure 3.3 and include a strip-loaded waveguide (Figure 3.3a), a ridge waveguide (Figure 3.3b), a rib waveguide (Figure 3.3c), a buried waveguide (Figure 3.3d), and a diffused waveguide (Figure 3.3e).

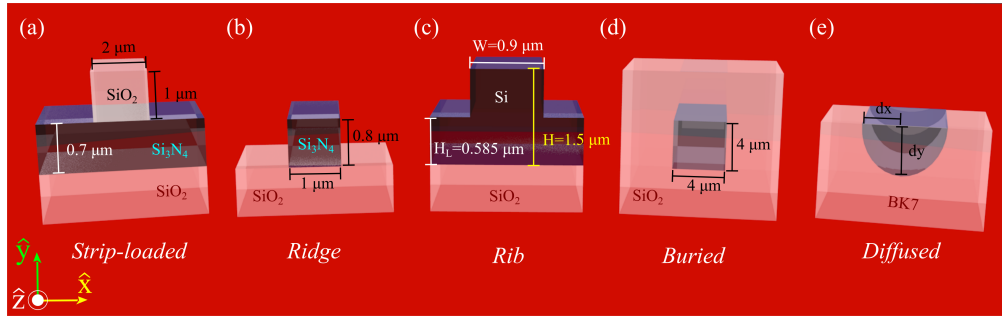


FIGURE 3.3: Rendered images of common laterally confined passive waveguide structures: (a) a strip-loaded waveguide, (b) a ridge waveguide, (c) a rib waveguide, (d) a buried waveguide, and (e) a diffused waveguide. The dimensions of the structures considered in this study are labeled.

We model the waveguides embedded in an index of refraction related to the mixture ratio 1:3 of N-Methylaniline to hexane which is:  $n(\lambda = 1.496\mu m) = 1.4299855 + j2.66917 \times 10^{-6}$ . Mixture ratio 1:3 of NMA:hexane was chosen to fulfill propagation criterion in a silica fiber. The strip-loaded waveguide (Figure 3.3a) was removed from the study because the strip is basically a spacer that separates the core and molecular mixture and prevents interaction.

We calculated the FoM for single-mode waveguides embedded in ratio 1:3 mixture of NMA:hexane for single-mode dimensions shown in Figure 3.3. Table 3.1 shows the fraction of the power in the core and in the analyte of SM waveguides embedded in a molecular 1:3 ratio mixture for a wavelength of  $1.5\mu m$ .

TABLE 3.1: Fraction of the power propagating in single-mode waveguide embedded in 1:3 ratio mixture of NMA:hexane for a wavelength of  $1.5 \mu m$  [1]

Waveguide type	quasi-TE		quasi-TM	
	$\eta_{\text{core}}$	FoM	$\eta_{\text{core}}$	FoM
ridge	0.868213	0.0868	0.858926	0.094387
slab	0.896623	0.050775	0.88289	0.056531
rib	0.991583	0.004672	0.992465	0.006981
diffused	0.99819	0.001783	0.998398	0.001603

Table 3.1 summarized the fraction of the power in the core and in the analyte. It shows that the max fraction of the power in the analyte is 9.4% for a ridge waveguide. For an efficient probing of the molecular layer, more than 10% of the power in the evanescent field in the analyte is required. Therefore, the waveguide design needs to be further optimized to obtain a higher FoM, which will increase the intensity and penetration depth of the evanescent field, resulting in a strong interaction with the surrounding medium. Squeezing the guiding layer is an elegant approach to increase the FoM and strengthen the interaction between the evanescent field and the molecular medium.

The single-mode dimension of each structure was minimized to half size while considering the fabrication limitations. This will increase the intensity and penetration depth of the evanescent field. This comparative study is aimed to provide a systematic comparison between different waveguide architectures by minimizing the physical dimensions of the structures with the same ratio. The buried waveguide changed to microfiber, which is the common configuration of buried waveguide.

Figures 3.4a-d show the calculated normalized electric field amplitudes of a slab, a rib, and a ridge squeezed waveguides, and of a microfiber, respectively [1].

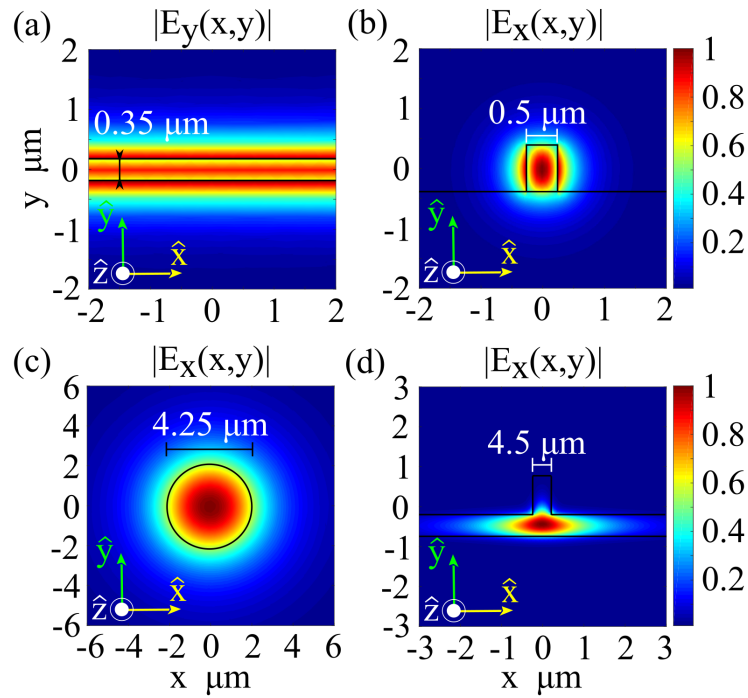


FIGURE 3.4: Normalized electric field amplitude colormaps for squeezed waveguides embedded in the mixture ratio 1:3 of NMA:hexane for a wavelength of  $1.5 \mu\text{m}$ : (a) slab waveguide, (b) rib waveguide, (c) ridge waveguide, and (d) microfiber.

Figure 3.4 shows the influence of a waveguide embedded in a 1:3 ratio mixture of N-methylaniline to hexane on the field distribution. Fig. 3.4a-d show the calculated normalized electric field amplitudes of slab, rib, and ridge waveguides, and of a microfiber, respectively. Squeezing of the physical dimensions of the guiding layer leads to increased evanescent field in the superstrate.

The FoM of the squeezed waveguides was calculated by using time average Poynting vector on COMSOL. Table 3.2 shows the fraction of the power in the core and in the analyte of squeezed waveguides embedded in a 1:3 ratio molecular mixture for a wavelength of  $1.5 \mu\text{m}$ .

TABLE 3.2: Fraction of the power carried by the modes of squeezed waveguides embedded in 1:3 ratio mixture of NMA:hexane for a wavelength of  $1.5 \mu\text{m}$  [1].

Waveguide		
type	$\eta_{\text{core}}$	FoM
ridge	0.598454	0.323221
slab	0.883412	0.056531
rib	0.978077	0.011161
fiber	0.67076	0.329247

Table 3.2 shows improvement in the fraction of the evanescent field in the analyte in ridge and microfiber. More than 30% of the power propagates in the analyte in those structures. Rib waveguides have smaller enhancement in the evanescent field, caused by the special configuration of the structure whose main purpose is to prevent interaction with the surface and reduce surface scattering losses.

Figures 3.5a-c [1] shows the evanescent fields extracted from the modes shown in Figures 3.4a, c, and d, respectively. These profiles are compared to the evanescent fields in the analyte in single-mode waveguides embedded in the molecular mixture.

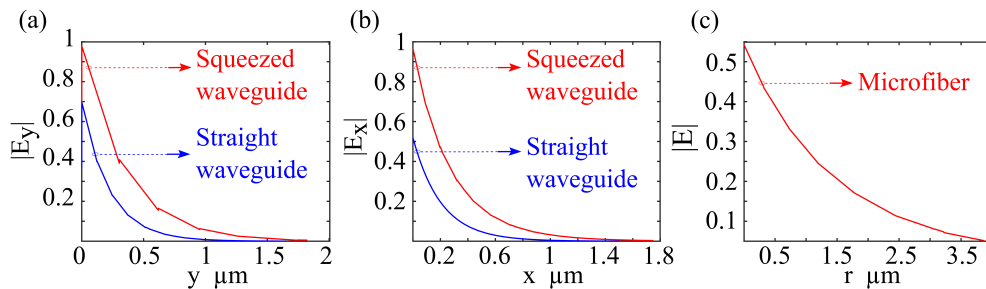


FIGURE 3.5: Cross-section profiles of normalized electric field amplitudes of the evanescent field in the analyte for squeezed waveguide compared to single-mode waveguides embedded in the mixture for a wavelength of  $1.5 \mu\text{m}$ . (a) Slab waveguide, (b) ridge waveguide, and (c) microfiber.

The amplitude of evanescent fields increases due to the squeezing of the guiding layer. However, according to Table 3.2, the FoM of the slab waveguide is too small ( $\sim 0.056$ ) for absorption overtone spectroscopy and, therefore, the tapered slab architecture is less favorable for sensing applications.

As shown in Table 3.2, the microfiber and the ridge waveguide are the best candidates for sensing. However, the ridge waveguide is preferable due to its roughness compared to the microfiber.

For the guiding medium, we chose silicon nitride -  $\text{Si}_3\text{N}_4$ . There are few reasons for choosing  $\text{Si}_3\text{N}_4$  for the guiding medium. The big advantage of  $\text{Si}_3\text{N}_4$  is its index of 1.98-2 in the NIR. It prevents limitation of checking samples with a high refractive index as derived from the guiding wave condition. For example, N-methylaniline, which has a refractive index around 1.57, can be checked with silicon nitride but not with tapered fiber, which has a lower refractive index ( $n_{\text{SiO}_2} = 1.445$ ). It also allows bigger dimensions for single-mode compared to silicon that allows for easier and low loss coupling.

Another advantage of  $\text{Si}_3\text{N}_4$  is low reflection losses compared to Si.  $\text{Si}_3\text{N}_4$  has a refractive index of 1.99 and Si of 3.48 around  $1.5 \mu\text{m}$ . In the interaction between the guiding layer and the air, a fraction of the power is reflected. Using Fresnel equation we can calculate the reflection.

$$R = \left| \frac{n_1 - n_2}{n_1 + n_2} \right|^2 \quad (3.7)$$

For Si the reflection is 30% and for  $\text{Si}_3\text{N}_4$  is 11%.

### 3.3 Waveguide design

As discussed in Chapter 2.4, tapered waveguide is the proposed structure for efficient overtone spectroscopy. The waveguide structure is an SM waveguide that is tapered in the middle of the guiding layer, as shown in Figure 3.6. The waveguide is covered with silica  $\text{SiO}_2$  except for a window in the sensing region. The cover limits the interaction between the evanescent field and the surroundings to the sensing area. It prevents any interaction with the environment in other regions, which disturbs the sampling.

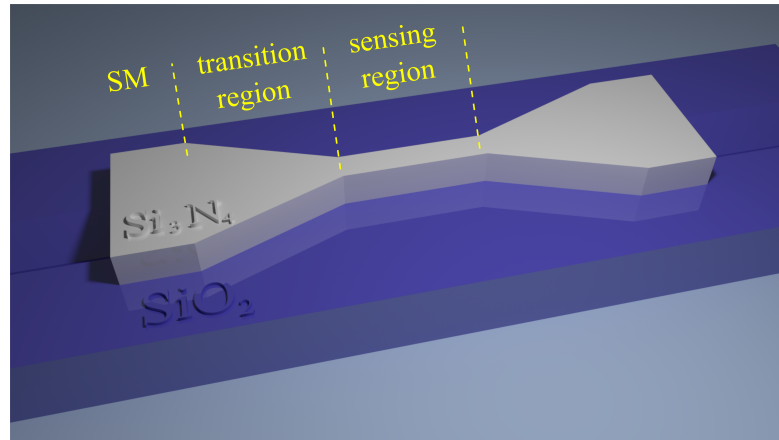


FIGURE 3.6: Schematic of ridge-tapered waveguide.

### 3.3.1 Single mode region

In the input and the output of the waveguide, a region with single-mode dimensions was chosen. The single-mode dimensions allow for easy coupling and easy light collection. Multi-mode dimensions can allow for better coupling. The drawback of a multi-mode waveguide is higher losses compared to a single-mode waveguide. Higher-order modes propagate at bigger inclination angles, result in higher surface scattering losses due to the large amount of reflections [14].

Using COMSOL, the dimensions of the SM region was calculated for wavelength range of 1.2-1.7  $\mu\text{m}$ . In the single-mode region, the guiding layer of silicon nitride is surrounded by silica. Due to the fabrication process, the height of the guiding layer needs to be 400 nm. To fulfill the single mode criterion, the width of the structure was calculated to be 700 nm.

### 3.3.2 Sensing region

We calculated the sensing region dimensions using COMSOL. We explored the fraction of the evanescent field for pure N-methylaniline and mixture ratio 1:3 of NMA:hexane for wavelength range of 1.2-1.7  $\mu\text{m}$ . We search for the width that will be narrow enough to enhance the fraction of the evanescent field but not too narrow, which results in stopping guiding the light.

We found that the optimal width for the sensing region is 350 nm.

Figure 3.7 shows the simulated absorption for the 350 nm width sensing region for N-methylaniline, hexane, and 2:3, 1:3, and 1:6 ratio mixtures of NMA:hexane calculated by Lumerical - Mode Solutions.

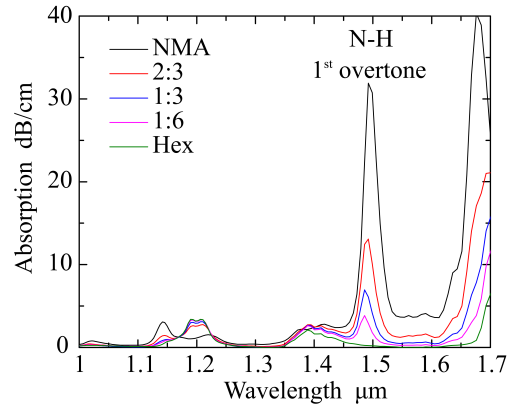


FIGURE 3.7: Absorption of hexane, N-methylaniline, and different ratio mixtures of NMA:hexane for a sensing region with a width of 350 nm.

The peak of the absorption is around  $1.49 \mu m$ , the absorption peak caused by the amine N-H bond first overtone. As the concentration of the N-methylaniline in the mixture decreases, the absorption gets smaller and shifts to shorter wavelengths.

In the next step, we checked propagation losses for the sensing area. As a result of thinning the sensing region the propagation losses increase, something that the calculation of the fraction of the evanescent field didn't show. For this part, we simulated the waveguide from the start to the start of the 2nd transition region. We calculated the transmission for the end of the sample. The sensing region length increases from  $15 \mu m$  to  $75 \mu m$  in interval of  $15 \mu m$ . The purpose is to find if the losses are stabilized after a certain length. This will show if the sample can be checked in this width.

Figure 3.8 shows the calculated losses of the sensing area for different lengths.

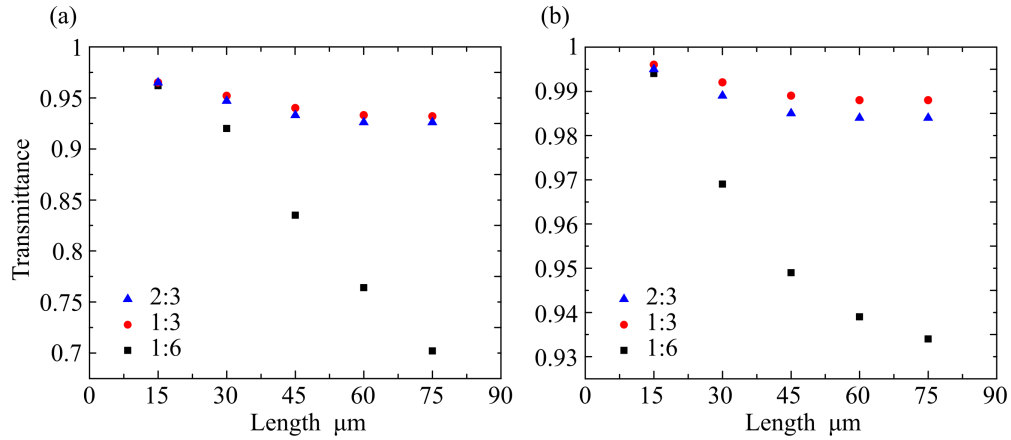


FIGURE 3.8: Propagation losses with different guiding layer widths for a wavelength of  $1.5 \mu\text{m}$  (a) width of 350 nm and (b) width of 400 nm.

In width of 350 nm (Figure 3.8a), the losses of mixture ratio 1:6 rise linearly as the sensing region lengthens while in mixture ratios 2:3 and 1:3 the losses stop increasing. This limits our waveguide for checking a variety of concentrations. In width of 400 nm (Figure 3.8b), the losses of mixture ratio 1:6 also stop increasing. As shown in Figure 3.8, broadening of the sensing region will allow using our waveguide for a wide range of mixtures and reduces the losses.

### 3.3.3 Transition region

The transition region is the area where the guiding layer tapers between the single-mode region to the sensing region. An important characteristic of the transition region is the need for adiabatic tapering. Adiabatic tapering requires a slow evolution along the taper. Adiabatic tapering eliminates any energy transfer between modes and reduces radiation loss [22, 27]. The tapering region needs to be long enough to be adiabatic but not too long, which will increase the propagation losses.

Another influence on the losses is the shape of the tapering, which influences the radiation losses. There are few tapering structures: linear (Figure 3.9a), parabolic (Figure 3.9b), hyperbolic (Figure 3.9c), and S-type (Figure 3.9d).

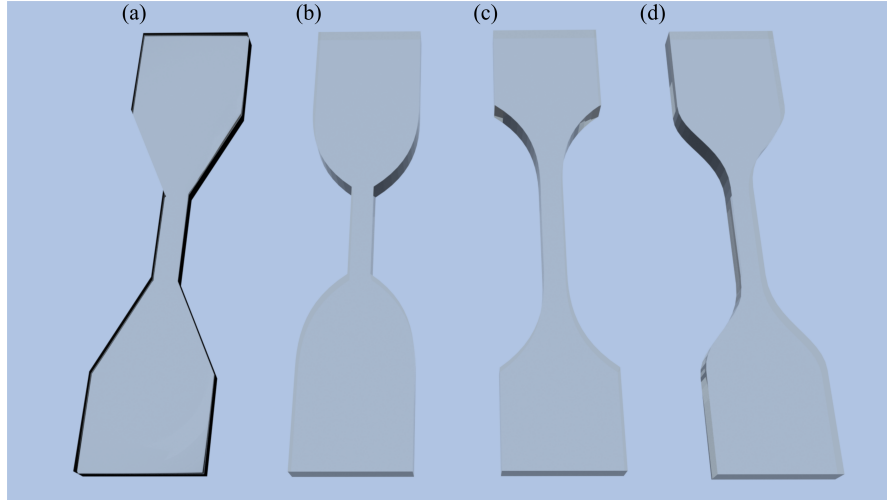


FIGURE 3.9: Different types of taper shapes: (a) linear, (b) parabolic, (c) hyperbolic, and (d) S-type.

The tapering shape that was chosen is S-tapering due to its low losses compared to the other shapes. We calculated the tapering length for minimal losses using Lumerical FDTD.

We found that the optimal length for the transition region is  $50 \mu m$ .

### 3.3.4 Calculated waveguide dimensions

- We calculated that the single-mode region dimensions are (W)  $700 \mu m \times$  (H)  $400 \mu m$ .
- We calculated that the optimal transition region is s-shape with length of  $50 \mu m$ .
- We calculated that the sensing area dimensions are (W)  $400 \mu m \times$  (H)  $400 \mu m$ .  
Wider sensing area allows checking variety of samples.

## Chapter 4

# Experimental results

### 4.1 Proof-of-principle experiments

#### 4.1.1 Spectroscopy of aromatic amines

We investigated the absorption of aromatic amines overtones using a Silicon rib waveguide.

Figure 4.1 shows the experimental set-up. We used a broadband laser source with a wavelength range of 400-2400 nm. The relevant range for our sensing is 1-1.7  $\mu m$ . The light is coupled into the single-mode. The fiber was held with a piezo-electric stage, which allows for precise adjustment of the fiber to the waveguide. The output signal was collected by multi-mode fiber into an optical spectrum analyzer.

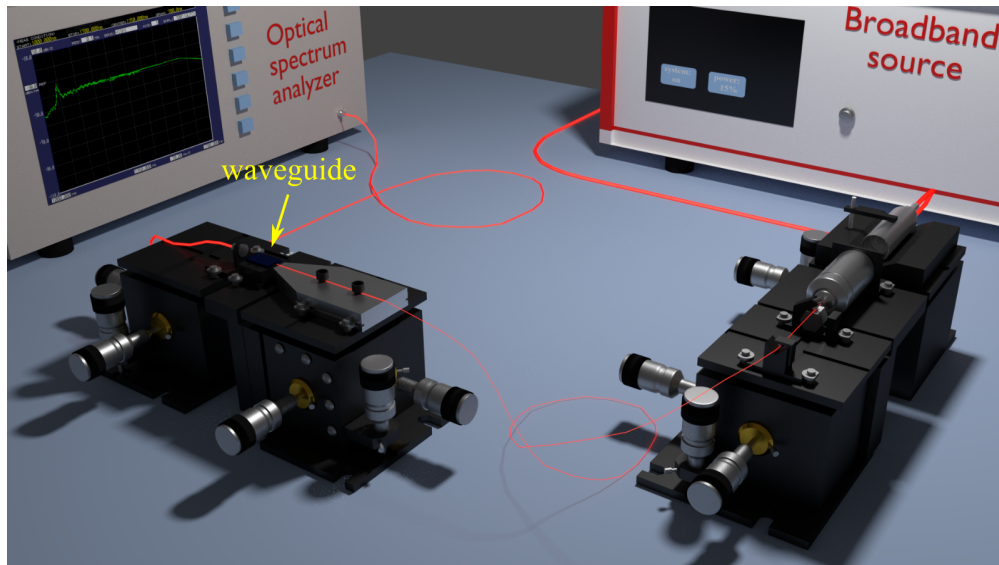


FIGURE 4.1: Schematic of the experimental set-up for in-line spectroscopic measurement.

Figure 4.2a shows schematic of the experiment. We dropped  $3 \mu\text{L}$  of the analyte onto the waveguide. The analytes were N-methylaniline, aniline, and mixtures of N-methylaniline with hexane. The strip is  $18 \mu\text{m}$  and  $0.4 \mu\text{m}$  height. Figure 4.2b shows the cross-section of the rib waveguide using a scanning electron microscope (SEM). A  $2 \mu\text{m}$  layer of  $\text{SiO}_2$  was placed above the silicon wafer to allow guidance.

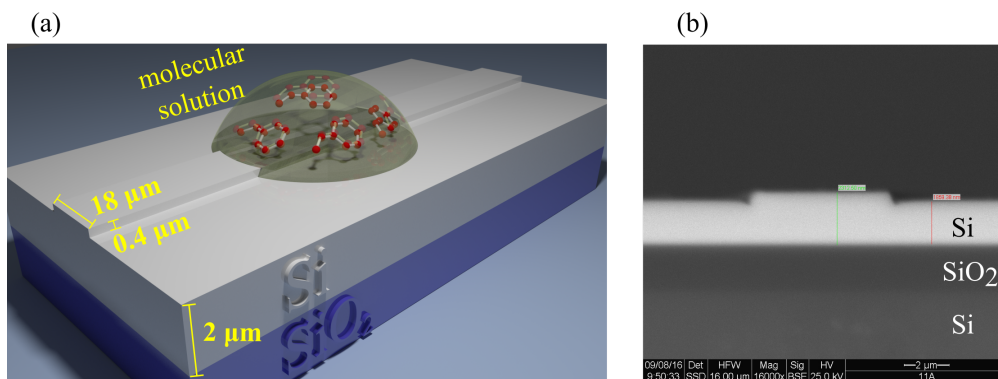


FIGURE 4.2: (a) Silicon rib waveguide used in the experiment. (b) Scanning electron micrograph (SEM) image of the waveguide cross-section.

Figure 4.3 shows the experiment results. Figure 4.3a shows the transmittance spectra of N-methylaniline and aniline molecules measured on Si rib waveguide. Figure 4.3b shows the transmittance spectra of the pure N-methylaniline molecule and 1:3 and 2:3 ratio mixtures of NMA:hexane measured on Si rib waveguide.

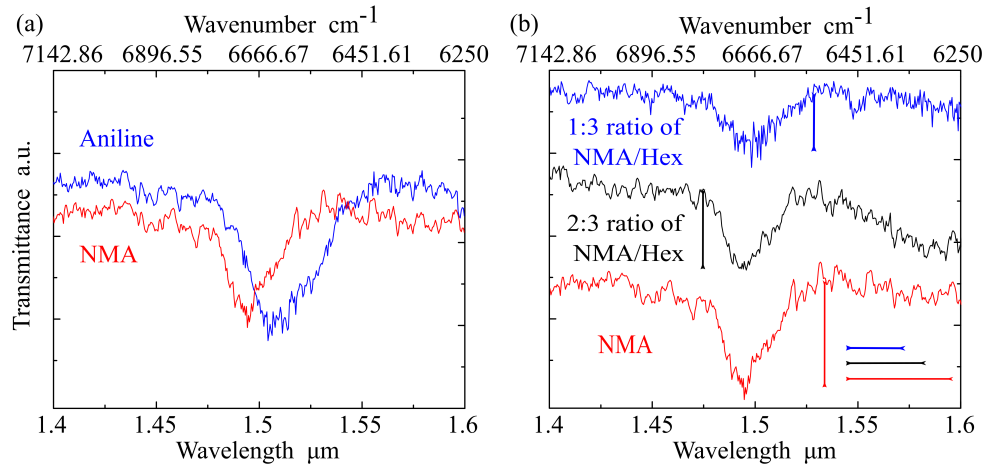


FIGURE 4.3: The transmittance spectra of different samples on silicon rib waveguide. (a) N-methylaniline and aniline. (b) N-methylaniline and mixture ratio 2:3 and 1:3 of NMA:hexane.

The experimental results, shown in Figure 4.3, clearly show the ability to distinguish between the mixtures of N-methylaniline and aniline. It shows that the absorption peak of the N-methylaniline and aniline is around 1.5  $\mu\text{m}$  as discussed previously. We can see that broadening of aniline absorption on the N-H first overtone, which results due to the combination modes [18, 20], as explained in Chapter 2.3. It also shows different transmittance for different mixtures of N-methylaniline and hexane. A lower concentration of N-methylaniline in the sample decreases the absorption bands, allowing distinguishing between the mixtures.

#### 4.1.2 Spectroscopy of cancer cell treatment response

We investigated the spectra changes before and after the treatment of ovarian cancer cells using tapered fiber.

In the experiment, the sensing device was microfiber. We tapered the fiber to approximately 2.5  $\mu\text{m}$  diameter using a commercial Vitran tapering system to increase evanescent field fraction. The fraction of the power in the evanescent field is approximately 8-15% due to fabrication tolerance. The major problem of using micro-diameter fiber is that it is very fragile and gentle. Also, it needs a lot of practice and effort to remove it from the tapering system. To overcome this problem, the tapered fiber was glued to a

metal fork, as shown in Figure 4.4b, while still connected to the tapering system. The metal fork allows moving the tapered fiber without harming it.

Another problem is checking the sample without harming the fiber. Dropping the sample onto the microfiber or touching the microfiber can result in breaking the fiber. For delicate placing of the sample on the microfiber we used Teflon bulk, which, due to its hydrophobic property, can be used as a liquid reservoir for the cancer cell. The sample was dropped on the Teflon and created a drop shape.

Figure 4.4a shows the experimental set-up for the cancer experiment. In the experiment, we used the set-up from the aromatic amine experiment. The waveguide was replaced with tapered fiber, as shown in Figure 4.4b. The tapered fiber was spliced to the coupled laser single-mode fiber using a fusion splicer. The output of the tapered fiber was collected into an optical spectrum analyzer. The cancer sample, volume of  $12 \mu\text{L}$ , was dropped onto the Teflon. The sample was gently slid to the microfiber region.

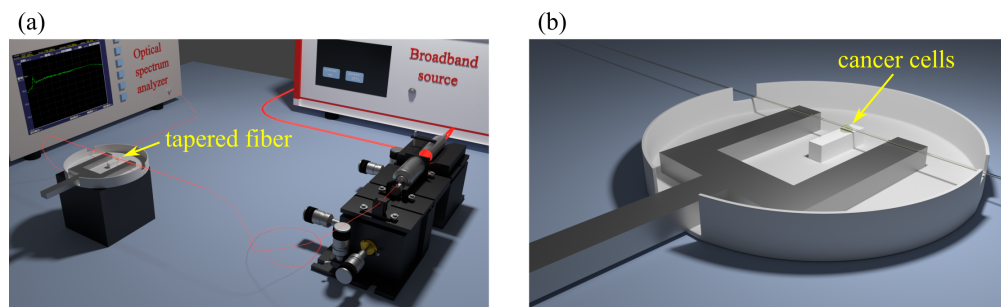


FIGURE 4.4: (a) Schematic of the experimental set-up. (b) Microfiber sensing device used in the experiment.

Figure 4.5 shows the cancer experiment result. Figure 4.5a shows the normalized transmittance of cancer cell with time difference of 30 sec. Figure 4.5a shows the transmittance spectra changes before and after 24h treatment in ovarian cancer cells.

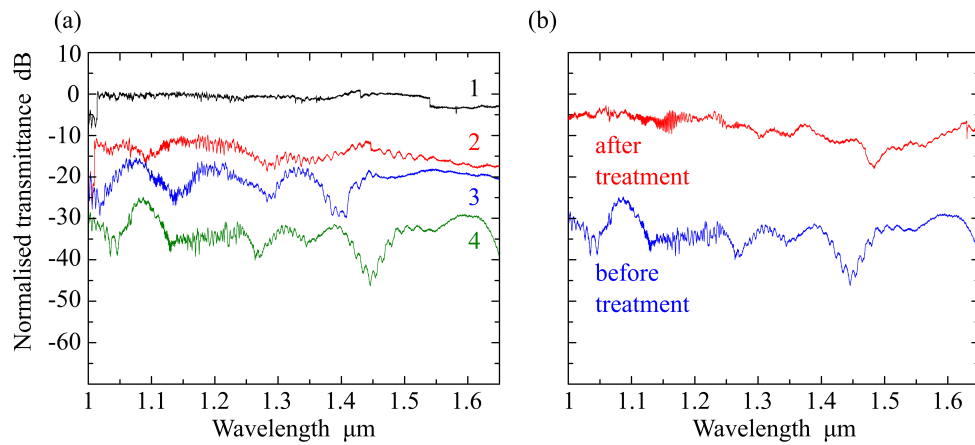


FIGURE 4.5: Normalized transmittance: (a) With time difference of 30 sec. (b) Before and after 24h treatment.

The experimental results, shown in Figure 4.5, clearly show a difference in transmittance spectra between the cancer cells before and after treatment. It shows smaller absorption by the cancer cell after the treatment, which can indicate about the treatment influence. It shows the cancer cell takes time to stick to the microfiber.

# Chapter 5

## Summary

### 5.1 Summary

We explored the wave propagation in different waveguide architectures theoretically for NIR region. We performed a comparative study of the evanescent field of those structures. We found that the fraction of the evanescent field in the analyte is very small in single-mode waveguide. Our approach to enhance the fraction was to squeeze the guiding layer. We found that the optimal structures to explore the effect of overtone absorption by broadband NIR illumination are squeezed ridge waveguide and microfiber. We calculated the optimal physical dimension of tapered ridge waveguide for overtone spectroscopy.

We proved the principle of vibration overtone spectroscopy on SOI rib waveguide. We detected the fingerprint of aromatic amines aniline and N-Methylaniline in the NIR, which results due to overtone vibration mode of N-H. In addition, we succeed to distinguish between different mixture of N-methylaniline and hexane by measuring the absorption of the first N-H overtones in each mixture.

We investigated the influence of treatment of ovarian cancer cells on tapered fiber. We found a difference in the transmission between ovarian cancer cells before and after 24h treatment. After treatment cancer cells have lower absorption compared to the cancer

cells without treatment, which can indicate about the treatment effect. This was a preliminary result that needs to be investigated for better understanding.

# Chapter 6

## Future plans

### 6.1 Future plans

- The preliminary results on detection cancer cells using microfiber shows a potential for cancer analysis. It needs a further investigating for better understanding of treatment influence on cancer cells with our technique.
- We simulated a tapered ridge waveguide for overtone absorption in the NIR. We will fabricate and investigate the tapered ridge waveguide structure.

## Chapter 7

# List of Publications

### 7.1 Journal articles

- [1] A. Katiyi, B. Hadad and A. Karabchevsky, *in Preparation*, "Broadband Near-Infrared Spectrometer Using Si Nanostrip Rib-Waveguide for Label-Free On-Chip Chemical Sensing".
- [2] A. Karabchevsky, A. Katiyi, M. I. M. Abdul Khudus and A. V. Kavokin, *Submitted 2017*, "Near-infrared spectroscopy of aromatic amines adsorbed on nanoparticles on reconfigurable microfibers: unexpected enhancement of absorption".
- [3] A. Katiyi and A. Karabchevsky, "Figure of merit of all-dielectric waveguide structures for absorption overtone spectroscopy", *Journal of Lightwave Technology* **35**, 1-7 (2017).

### 7.2 Conference papers

- [1] A. Katiyi and A. Karabchevsky, "Nano-tapers: squeezing light in a dielectric nano-guide for overtone spectroscopy", *MetaNano, Anapa, Russia* 5 - 9 Sep 2016. Invited Talk.
- [2] A. Katiyi, B. Hadad and A. Karabchevsky, "Silicone Waveguides for Broadband overtone spectroscopy of N-Methylamine and Aniline in near-infrared", *OASIS6, Tel Aviv, Israel* 27-28 Feb 2017.

# References

- [1] A. Katiyi and A. Karabchevsky, “Figure of merit of all-dielectric waveguide structures for absorption overtone spectroscopy,” *Journal of Lightwave Technology* **35**, 1–7 (2017).
- [2] W. S. Struve, *Fundamentals of molecular spectroscopy* (Wiley New York, 1989).
- [3] B. Suart, *Infrared Spectroscopy: Fundamental and Applications* (John Wiley & Sons, Ltd, 2004).
- [4] M. Reichenbacher and J. Popp, *Challenges in molecular structure determination* (Springer Science & Business Media, 2012).
- [5] G. Reich, “Near-infrared spectroscopy and imaging: basic principles and pharmaceutical applications,” *Advanced drug delivery reviews* **57**, 1109–1143 (2005).
- [6] P. A. Anderson, B. S. Schmidt, and M. Lipson, “High confinement in silicon slot waveguides with sharp bends,” *Optics Express* **14**, 9197–9202 (2006).
- [7] P. T. Lin, S. W. Kwok, H.-Y. G. Lin, V. Singh, L. C. Kimerling, G. M. Whitesides, and A. Agarwal, “Mid-infrared spectrometer using opto-nanofluidic slot-waveguide for label-free on-chip chemical sensing,” *Nano letters* **14**, 231–238 (2013).
- [8] R. Siebert and J. Müller, “Infrared integrated optical evanescent field sensor for gas analysis: part I: system design,” *Sensors and Actuators A: Physical* **119**, 138–149 (2005).
- [9] W. Bogaerts, P. De Heyn, T. Van Vaerenbergh, K. De Vos, S. Kumar Selvaraja, T. Claes, P. Dumon, P. Bienstman, D. Van Thourhout, and R. Baets, “Silicon microring resonators,” *Laser & Photonics Reviews* **6**, 47–73 (2012).
- [10] A. Nitkowski, L. Chen, and M. Lipson, “Cavity-enhanced on-chip absorption spectroscopy using microring resonators,” *Optics express* **16**, 11 930–11 936 (2008).
- [11] A. Karabchevsky and A. Kavokin, “Giant absorption of light by molecular vibrations on a chip,” *Scientific Reports* **6** (2016).

- 
- [12] P. L. Huyskens, W. A. Luck, and T. Zeegers-Huyskens, *Intermolecular forces: an introduction to modern methods and results* (Springer Science & Business Media, 2012).
- [13] H. F. Taylor and A. Yariv, “Guided wave optics,” *Proceedings of the IEEE* **62**, 1044–1060 (1974).
- [14] R. G. Hunsperger, *Integrated optics: theory and technology* (Springer, 2009).
- [15] A. Karabchevsky, J. S. Wilkinson, and M. N. Zervas, “Transmittance and surface intensity in 3D composite plasmonic waveguides,” *Optics Express* **23**, 14 407–14 423 (2015).
- [16] A. Skumanich and C. R. Moylan, “The vibrational overtone spectrum of a thin polymer film,” *Chemical Physics Letters* **174**, 139–144 (1990).
- [17] W. Groh, “Overtone absorption in macromolecules for polymer optical fibers,” *Die Makromolekulare Chemie* **189**, 2861–2874 (1988).
- [18] K. B. Whetsel, W. E. Roberson, and M. Krell, “Near-infrared spectra of primary aromatic amines,” *Analytical Chemistry* **30**, 1598–1604 (1958).
- [19] Z. Rappoport, *The chemistry of anilines*, Vol. 169 (John Wiley & Sons, 2007).
- [20] S. Shaji and T. Rasheed, “Vibrational overtone spectra of chloroanilines—evidence for intramolecular hydrogen bonding in o-chloroaniline,” *Spectrochimica Acta Part A: Molecular and Biomolecular Spectroscopy* **57**, 337–347 (2001).
- [21] S. Shaji, S. M. Eappen, T. Rasheed, and K. Nair, “NIR vibrational overtone spectra of N-methylaniline, N, N-dimethylaniline and N, N-diethylaniline—a conformational structural analysis using local mode model,” *Spectrochimica Acta Part A: Molecular and Biomolecular Spectroscopy* **60**, 351–355 (2004).
- [22] G. Brambilla, “Optical fibre nanowires and microwires: a review,” *Journal of Optics* **12**, 1–19 (2010).
- [23] A. Karabchevsky, A. Katiyi, M. I. M. Abdul Khudus, and A. V. Kavokin, “Near-infrared spectroscopy of aromatic amines adsorbed on nanoparticles on reconfigurable microfibers: unexpected enhancement of absorption,” Submitted 2017 .
- [24] V. Lucarini, J. J. Saarinen, K.-E. Peiponen, and E. M. Vartiainen, *Kramers-Kronig relations in optical materials research*, Vol. 110 (Springer Science & Business Media, 2005).

- 
- [25] J. E. Bertie and S. L. Zhang, “Infrared intensities of liquids. IX. The Kramers–Kronig transform, and its approximation by the finite Hilbert transform via fast Fourier transforms,” *Canadian Journal of Chemistry* **70**, 520–531 (1992).
- [26] K. Okamoto, *Fundamentals of optical waveguides* (Academic press, 2010).
- [27] C. T. Lee, M. L. Wu, L. G. Sheu, P. L. Fan, and J. M. Hsu, “Design and analysis of completely adiabatic tapered waveguides by conformal mapping,” *Journal of lightwave technology* **15**, 403–410 (1997).